Laser and Particle Beams (2001), *19*, 481–495. Printed in the USA.

Zero-dimensional energetics scaling models for *z*-pinch-driven hohlraums

M.E. CUNEO,[1] R.A. VESEY,[1] J.H. HAMMER,[2] J.L. PORTER, JR.,[1] L.E. RUGGLES,[1] AND W.W. SIMPSON[1]

[1]Sandia National Laboratory, Albuquerque, NM 87185-1193, USA
[2]Livermore National Laboratory, Livermore, CA 94551, USA

(RECEIVED 22 May 2000; ACCEPTED 20 April 2001)

Abstract

Wire array *z* pinches on the Z accelerator provide the most intense laboratory source of soft X rays in the world. The unique combination of a near-Planckian radiation source with high X-ray production efficiency (10 to 15% wall plug), large X-ray powers and energies (>100 TW, ≥0.8 MJ in 6 ns to 7 ns), large characteristic hohlraum volumes (0.5 to >10 cm^3), long pulse lengths (5 to 20 ns), and low capital cost (<$50–$100/radiated Joule) may make *z* pinches a good match to the requirements for driving high-yield scale (>200 MJ yield) ICF capsules with adequate radiation symmetry and margin. The *z*-pinch-driven hohlraum approach of Hammer *et al*. (1999) may provide a conservative and robust solution to the requirements for high yield, and is currently being studied on the Z accelerator. This paper describes a multiple-region, 0-D hohlraum energetics model for *z*-pinch-driven hohlraums in four configurations. We observe consistency between the model and the measured X-ray powers and hohlraum wall temperatures to within ±20% in X-ray flux, for the four configurations. The scaling of pinch energy and radiation-driven anode-cathode gap closure with drive current are also examined.

1. INTRODUCTION

Tungsten wire array (Sanford *et al.*, 1996; Deeney *et al.*, 1997) *z* pinches on the Z-driver (Spielman *et al.*, 1998) have recently found many applications to driving high-temperature radiation cavities or hohlraums. The unique combination of a near-Planckian radiation source with high X-ray production efficiency (10 to 15% wall plug), large X-ray powers and energies (>100 TW, >0.8 MJ in 6 ns to 7 ns), large characteristic hohlraum volumes (0.5 cm^3 to > 10 cm^3), long pulse lengths (5 ns to 20 ns), and low capital cost (<$50–$100/radiated Joule) may make *z*-pinches a good match to the requirements for driving high-yield scale (>200-MJ yield) ICF capsules with adequate radiation symmetry and margin. Assessment of *z* pinches for high-yield ICF is one of the goals of the research program at Sandia National Laboratories. Three different geometries are being studied to harness *z*-pinches for indirect-drive ICF: the dynamic hohlraum (Lash *et al.*, 2000; Nash *et al.*, 1999; Slutz *et al.*, 2001), static-wall hohlraum (Olson *et al.*, 1999; Sanford *et al.*, 1999, 2000), and *z*-pinch-driven hohlraum (Porter, 1997; Vesey *et al.*, 1998, 1999; Baker *et al.*, 1999, 2000; Cuneo *et al.*, 1999*a*, 1999*b*, 2000, 2001; Hammer *et al.*, 1999). Each of these approaches has a fundamentally different drive geometry, and hence different potential strengths and concerns, which have been previously described (Matzen *et al.*, 1997, 1999; Leeper *et al.*, 1999). This article describes a 0-D hohlraum energetics model to relate pinch X-ray power to hohlraum wall temperatures for four *z*-pinch-driven hohlraum configurations. The scaling of pinch energy and radiation-driven anode-cathode gap closure with drive current are also examined.

The *Z*-Pinch-Driven Hohlraum (ZPDH) concept is depicted in Figure 1. In this concept, *z* pinches are located in two primary radiation cavities or source hohlraums on either end of a secondary radiation cavity or capsule hohlraum. A wire array consisting of many hundreds of fine tungsten wires is located in each primary. Electromagnetic power enters each primary through a small (≈2 mm) annular anode-cathode (AK) gap at the base of the wire array. The AK gaps are coupled to a single pulsed-power driver through their own set of low-inductance transmission lines (Spielman *et al.*, 1998) which deliver large currents to the wire arrays. The wire arrays are accelerated towards the axis of the hohlraum by the applied current. The kinetic energy of the wire array as well as additional magnetic energy is observed to be rapidly and efficiently thermalized and converted to soft

Address correspondence and reprint requests to: M.E. Cuneo, Sandia National Laboratory, Albuquerque, NM 87185-1193, USA. E-mail: mecuneo@sandia.gov

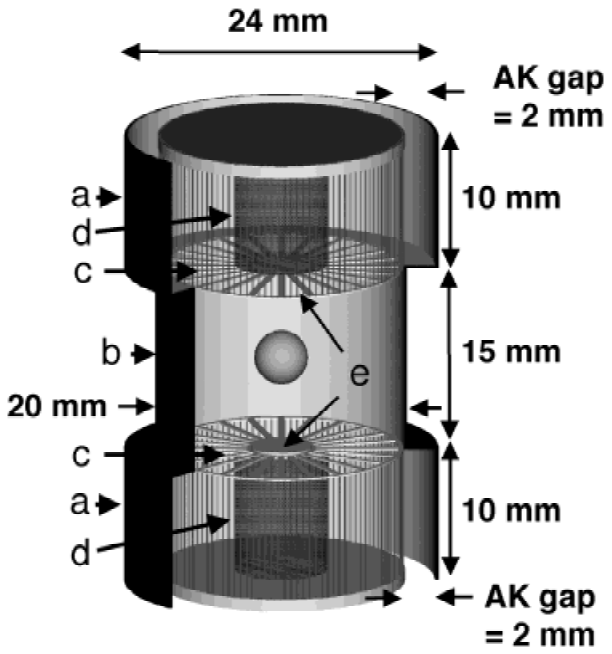

Fig. 1. High yield *z*-pinch-driven hohlraum configuration, that is, a double-sided power feed, double-sided secondary showing (a) two 24×10 mm^2 primaries or X-ray source hohlraums with 300 11.5-μm-diameter W wire arrays including two AK-gap power feeds, (b) 20×15 mm^2 secondary with 5-mm-diameter high yield capsule, (c) two Be spoke assemblies, (d) two foam pulse-shaping cylinders on axis in the primaries, and (e) two 5-mm-diameter axial shine shields. The pinch stagnates on the axis of the primary hohlraum. These *z*-pinch primaries are each driven by a separate set of transmission lines. Current smoothing between these lines is performed in the output section of the accelerator over a large number of individual accelerator modules to provide identical current pulses to the two pinches (Struve *et al.*, 1999).

X rays as the mass stagnates against itself on axis, heating up the primary hohlraum. The radiation field in the hohlraum is enhanced by making the walls out of a high-Z material, which efficiently re-radiates and traps the X-ray power (Lindl, 1995). Furthermore, the *z* pinch implodes onto an additional wire array or central foam target to provide the required radiation drive pulse shape for the capsule implosion. This pulse-shaping concept has been demonstrated experimentally, in principle (Hammer *et al.*, 1999; Sanford *et al.*, 2000).

The majority of the secondary hohlraum X-ray drive comes from re-radiation of the primary wall (more than 70% of the X-ray flux entering the secondary, according to the viewfactor models discussed below). Less than 30% of the secondary wall drive comes from direct-pinch illumination. This topology of coupling two, hot X-ray source regions to a cooler, ICF secondary is similar to some indirectly driven laser hohlraum geometries (Lindl, 1995; Rosen, 1996). Radiation flows into the secondary through Be-spoke assemblies which are largely transparent to X rays, and which also act to carry the *z*-pinch current, as well as confine the *z*-pinch plasma to the primary region. The mass per unit area of this spoke array must be large enough to prevent significant $\mathbf{J} \times \mathbf{B}$-driven axial motion in order to maintain good transparency. Experimentally, these Be spokes are observed to maintain their spoke-like character throughout the power pulse giving efficient X-ray transport from primary to secondary hohlraum in between the spoke material (Hammer *et al.*, 1999; Cuneo *et al.*, 2001). These spokes impose a high-order azimuthal mode effect on radiation symmetry, that the capsule can tolerate (Hammer *et al.*, 1999). Future experiments will evaluate the degree of MHD-coupling of pinch plasma into the secondary hohlraum, through the spokes.

The *z*-pinch-driven-hohlraum configuration theoretically provides the 1% capsule X-ray flux uniformity required for high convergence implosions according to viewfactor simulations discussed below (Vesey *et al.*, 1998, 1999; Hammer *et al.*, 1999). The two-sided ZPDH system in Figure 1 provides the most conservative approach to control of symmetry for a *z*-pinch-driven system. As noted, this concept provides two levels of radiation smoothing over the millimeter-scale-length pinch spatial nonuniformities typical of *z* pinches: primary hohlraum wall re-emission followed by secondary hohlraum wall re-emission. Symmetry is obtained geometrically in a ZPDH by overlapping the primary and secondary radiation sources onto the capsule to create a uniform drive (Vesey *et al.*, 1998, 1999; Hammer *et al.*, 1999). The possibility of geometric symmetry control is permitted because the pinch is an extended radiator. Laser-driven systems develop extended radiators on the hohlraum walls by phasing different groups of laser beams over the surface of a cylindrical hohlraum in order to compensate for the nonspherical hohlraum geometry, wall motion and the laser entrance hole (Lindl, 1995). Secondary hohlraum radiation symmetry of even modes (e.g., P2, P4, P6, etc.) is provided by altering the length and diameter of the secondary (and primary), as well as by varying the diameter and location of an axial shine shield, which prevents a pole-hot capsule drive (Vesey *et al.*, 1998, 1999). Figure 1 shows a particular example with the secondary diameter the same as the wire array diameter. High-yield capsules of 5-mm diameter probably require a secondary diameter of 15 mm to 20 mm for adequate control of symmetry. The large hohlraum size reduces sensitivity to wall motion. Symmetry can also be tuned by altering the shape of the secondary walls away from a purely cylindrical geometry with constrained flux optimization techniques (Vesey *et al.*, 1998, 1999). Radiation symmetry of odd modes (P1, P3, and P5) is controlled with adequate power balance and timing simultaneity for the two *z* pinches (Vesey *et al.*, 1998, 1999; Hammer *et al.*, 1999; Cuneo *et al.*, 2001). Coupling to higher order odd modes (P3 and P5) appears to be tolerable. Control of P1 asymmetry is the principal concern. *Z*-pinch driven systems are also expected to have a high degree of cylindrical symmetry.

Experiments have shown that this scheme for coupling radiation to a secondary is practical and efficient (Cuneo *et al.*, 1999*a*, 1999*b*, 2000, 2001). Experiments are building

https://doi.org/10.1017/S0263034601193055 Published online by Cambridge University Press

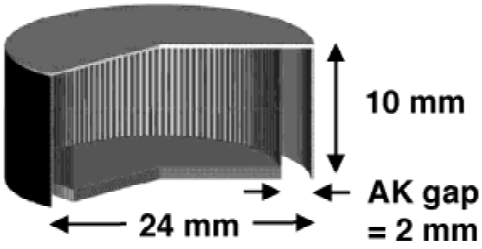

Fig. 2. The $24 \times 10\text{-mm}^2$ *z*-pinch-driven primary hohlraum configuration. This configuration smooths the pinch radiation and provides a large surface area to drive 3 to 12 side-viewing experimental packages with very similar radiation histories (Porter, 1997). This primary is also used to drive large diameter secondaries for the high-yield ICF concept. This configuration can be used to study hohlraum and pinch energetics, power flow physics, pulse shaping, and reproducibility.

in complexity towards the desired configuration in Figure 1. Experiments have studied the energetics of *z*-pinch-driven primaries (Porter, 1997; Baker *et al.*, 1999; see Fig. 2). Hohlraum and pinch energetics, radiation coupling, and average transparency of Be-spokes were studied in a single-sided primary-secondary configuration (Cuneo *et al.*, 1999*a*, 1999*b*, 2001; see Fig. 3). The power flow, pinch and hohlraum energetics, pinch power balance, and simultaneity of a single-sided power feed, double-pinch driven secondary were also studied (Cuneo *et al.*, 2000, 2001; see Fig. 4). Section 2 of this paper briefly describes the diagnostics used to obtain pinch X-ray powers and hohlraum temperature measurements. Section 3 describes a 0-D hohlraum energetics model for the *z*-pinch-driven hohlraums in each of the four configurations which establishes consistency between measured X-ray powers and hohlraum wall temperatures. These models are similar in nature to those developed for laser hohlraums (Lindl, 1995; Rosen, 1996), and to earlier work on

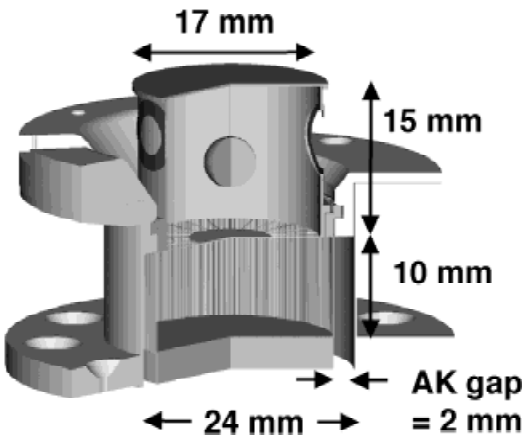

Fig. 3. *Z*-pinch-driven single-sided secondary hohlraum configuration. A $24 \times 10\text{-mm}^2$ primary drives a $17 \times 15\text{-mm}^2$ secondary through a 17-mm-diameter Be spoke assembly, providing an experimental geometry for measuring hohlraum energetics, spoke transparency, radiation coupling, MHD isolation of the secondary from the primary, azimuthal drive asymmetry, and capsule preheat.

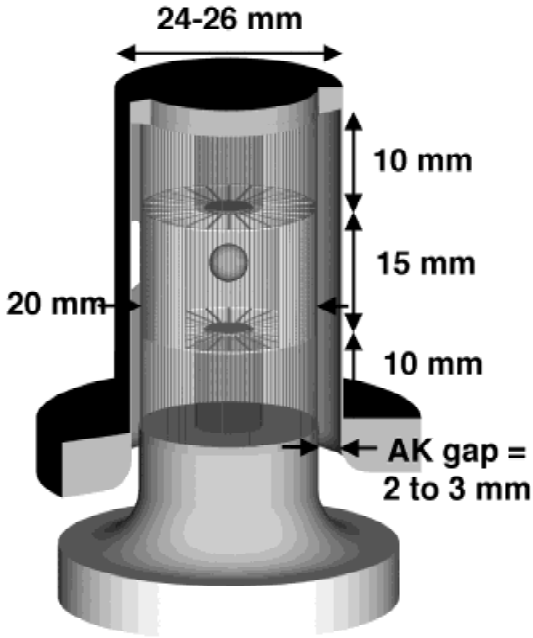

Fig. 4. Single-sided power feed, double-sided secondary hohlraum configuration used to study radiation symmetry, pinch power balance and simultaneity, and capsule implosions on the Z accelerator, prior to the development of an accelerator configuration with a two-sided feed architecture (e.g., see Fig. 1). The secondary is suspended off of the tungsten wires and becomes part of the power feed to supply current to the upper pinch.

z-pinch-driven hohlraums (Hammer *et al.*, 1999). These models allow us to identify possible breakpoints in physics issues and driver performance, quickly evaluate experiments, and plan an organized research program. Section 4 summarizes the hohlraum scaling models. Based on these models, the energetics of the ZPDH appears to scale to the required high-yield temperatures for a two-sided system (Fig. 1) if the X-ray power output of each pinch can be scaled to about 1000–1200 TW depending on the amount of AK gap closure. Two-dimensional radiation hydrodynamics (2-D RMHD) simulations show this range of pinch power for currents of order 60 MA (Hammer *et al.*, 1999). Appendix A describes a 0-D model for pinch energy scaling with tungsten pinch mass and drive current and compares the results with 2-D RMHD simulations. Appendix B describes a simple scaling for magnetic tamping of radiation-driven closure of the AK feed gap. Table 1 lists the key areas that are being studied to qualify this approach for high-yield fusion in our research program at Sandia. We will be able to study all of these issues with one of these four hohlraum configurations.

2. DIAGNOSTICS

Hohlraum wall re-emission temperatures and pinch X-ray powers are measured by several different types of X-ray detectors through apertures in the hohlraum wall [XRDs (Chandler *et al.*, 1999), ns-response Bolometers (Spielman

https://doi.org/10.1017/S0263034601193055 Published online by Cambridge University Press

Table 1. *Physics issues for high yield assessment.*

Issue	Comments
Pinch energetics	Demonstrate the scaling of pinch output with mass, current, and atomic number to provide the required X-ray power.
Power flow	Demonstrate scaling of radiation and current-driven closure of the magnetically tamped power feed gap to provide the power to the pinch at higher temperatures and currents.
Hohlraum energetics	Establish the relationship between X-ray power and hohlraum temperature.
Radiation coupling	Determine the efficiency of transport of radiation into the secondary, and Be spoke transparency.
Pinch power balance	Demonstrate power balance between two primaries to control P1 on a capsule in the secondary.
Pinch power simultaneity	Demonstrate power timing between two primaries to control P1 swing on a capsule in the secondary.
Polar radiation symmetry	Demonstrate geometric control of even mode radiation symmetry for a capsule in the secondary.
Azimuthal symmetry	Characterize azimuthal radiation symmetry for a capsule in the secondary.
MHD isolation	Assess and control of expansion of pinch plasma into the secondary.
Capsule preheat	Assess and control levels of plasma, high-energy particle and radiation preheat.
Pulse shaping	Demonstrate control of radiation pulseshape adequate for high-yield capsule and quantify energetics, timing, and reproducibility.
Capsule energetics	Design of capsules with large radius, fuel mass, and appropriate stability.
Capsule implosions	Use capsule implosions to assess symmetry to ICF relevant levels.

et al., 1999), and Transmission Grating Spectrometers (Ruggles *et al.*, 2001)]. The aperture size is measured with time-resolved, filtered X-ray framing cameras to correct both wall re-emission flux, and pinch X-ray flux for aperture closure (Chrien *et al.*, 1999; Baker *et al.*, 2000). Initial aperture sizes of 12.6 mm^2 to 16 mm^2 close by about 50% in primaries and about 35% in secondaries. Uncertainty in the wall re-emission flux and pinch X-ray measurements is $\pm 20\%$ ($\pm 5\%$ in temperature), adding uncertainties in aperture closure and instrumental calibration in quadrature. This is comparable to temperature uncertainties for laser hohlraums (Lindl, 1995). Load currents are measured with B-dot loops (Stygar *et al.*, 1997).

3. HOHLRAUM ENERGETICS MODELS

In these 0-D models, we write coupled equations, which balance the power sources and sinks for each hohlraum in the system (Lindl, 1995; Rosen, 1995, 1996, 1999). A recent article reviews and extends the basis of these kinds of models (Stygar *et al.*, 2001). The power balance equations for each hohlraum (primary or secondary) have the form of power input = power loss, or source = sink.

3.1. Primary only

The power balance equation in the case of a single primary (Fig. 2) is

$$P_p = [(1-\alpha_p)A_{wp} + A_{hp} + (1-\alpha_g)A_g]\sigma T_p^4 = A_p \sigma T_p^4, \quad (1)$$

where P_p is the net pinch X-ray power (source) and A_p is the effective loss area for the hohlraum (sink), α_p and α_g are albedos (X-ray re-emissivities) for the Au hohlraum wall, and the anode-cathode (AK) gap transmission line power feed respectively, A_{wp}, A_{hp}, and A_g are the areas for the gold hohlraum wall, the diagnostic apertures, and the AK gap, T_p is the temperature of the radiation field incident on the hohlraum surfaces, and σ is the Stefan–Boltzmann constant. Radiation is lost diffusively into the Au hohlraum wall, and free-streams out diagnostic apertures, and out the AK gap. Some of the X rays streaming out the AK gap are returned back into the hohlraum by the transmission line feed structure. Albedos are defined as $\alpha = P_{out}/P_{in}$, the ratio of re-emitted X-ray power to incident X-ray power (Rosen, 1995). Most of the "physics" for this model is contained in the proper choices for albedos. The AK gap is an additional radiation leak (like a diagnostic aperture) somewhat like the laser entrance hole in a laser-driven system. The effective albedos for the AK gaps are provided by 3-D viewfactor simulations (Vesey *et al.*, 1998, 1999). This allows a calculation of the net X-ray return to the hohlraum from the transmission line feed. The main energy sink for hohlraums is the X-ray energy diffusively deposited in the Au wall that is not re-emitted. The incident X rays drive a radiation heat-diffusion wave (a "Marshak wave") into the wall (Rosen, 1995, 1996, 1999). High-Z materials have a high re-emissivity (≈ 0.8) of X rays once they become hot, and the gradient driving energy into the wall flattens near the surface. Thus, hohlraums typically use gold walls to confine the X-ray flux in a high re-emission cavity. The hohlraum Au wall albedos are a strong function of peak temperature and temperature history or pulse shape. In previous work, the wall loss (or equivalently wall albedo) was described by an analytic formulation (Lindl, 1995; Rosen, 1995, 1996, 1999), that was a good description of the diffusion of X-ray energy into the hohlraum wall, for pulse shapes typical of laser hohlraums. In this work, the Au wall albedos are provided by 1-D radiation hydrodynamics (RMHD) calcula-

https://doi.org/10.1017/S0263034601193055 Published online by Cambridge University Press

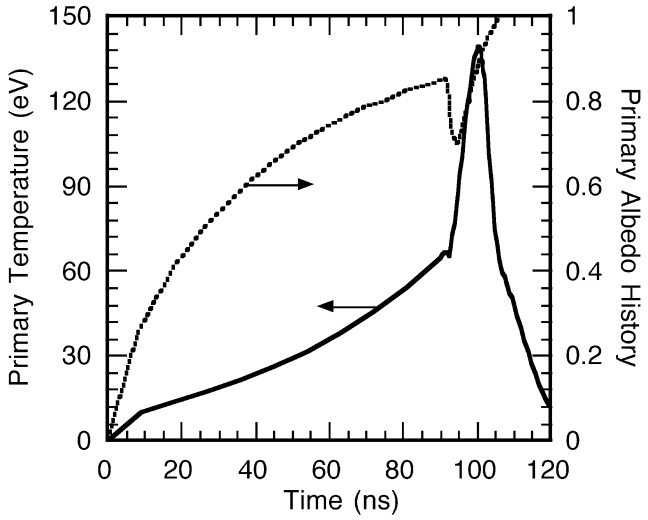

Fig. 5. Example primary temperature pulse (solid line) and calculated Au wall albedo history (dotted line) derived from 1-D RMHD simulations.

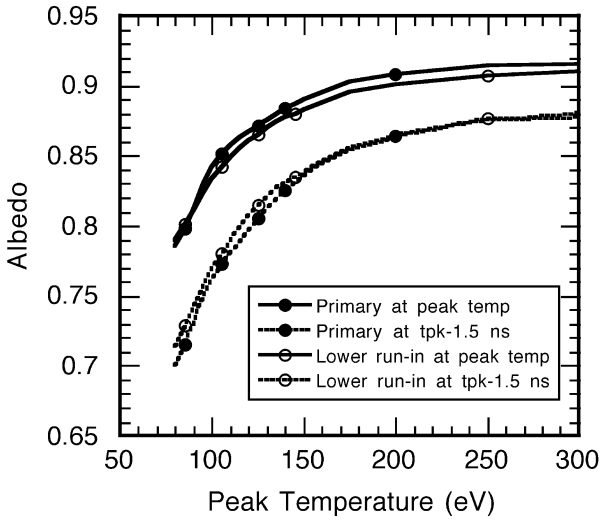

Fig. 6. Calculated albedos *versus* peak temperatures: at peak temperature (solid circles/solid lines) and 1.5 ns prior to peak temperature (solid circles/dotted lines), for primary temperature pulse shapes, and pulses with about a factor of 2 lower run-in temperature (open circles).

tions with the Lasnex code (Zimmerman & Kruer, 1975) using STA opacity tables (Bar-Shalom *et al.*, 1989).

An example radiation temperature pulse shape for a primary is shown in Figure 5, with the corresponding calculated albedo history. The temperature history in Figure 5 is representative of simulations (Chrien *et al.*, 1999) before 75 ns, and measurements after 75 ns (Porter, 1997; Cuneo *et al.*, 1999*b*, 2000, 2001). The temperature up until 90 ns results from pinch radiation during its run-in or acceleration phase. Run-in radiation lowers the albedo (at peak) by pre-expanding the Au-hohlraum wall. Run-in radiation increases the albedo slightly, 1.5 ns before peak. However, the albedos near peak temperature are insensitive to the temperature history of the pinch run-in phase (see Fig. 6); lack of run-in radiation would only change the albedo by $<+3\%$. The inflection points in the albedo correspond to inflection points in the temperature history. In particular, note that the albedo decreases at the transition point between the pinch-run in and the rapid temperature rise during the main X-ray pulse at pinch stagnation. The rapid increase in temperature increases the gradient driving energy into the wall for a short period, lowering the albedo. The albedo is artificially clamped at 1 in these simulations. The hohlraum wall can become a net radiator, returning its energy to the system at some point as the input power falls, which would give an albedo greater than 1 by the above definition.

One- and two-dimensional RMHD simulations of *z*-pinch-driven hohlraums show a 1.5-ns timing delay between the peak pinch power and the peak temperature. In our 0-D treatment, we look for consistency between the peak pinch power, the temperature 1.5 ns before peak, and the albedo 1.5 ns prior to peak temperature. One might also look for consistency with the peak temperature (and albedo) with the pinch power 1.5 ns after peak pinch power. Experimentally we measure a timing delay between peak pinch and peak temperature of 2 ± 1 ns. Figure 6 plots the albedos 1.5 ns prior to peak temperature, and at peak temperature for the primary temperature pulse shape shown in Figure 5, as the peak temperature is changed. Figure 6 also plots similar albedos for a temperature pulse with a factor of two lower temperature during the run-in phase, showing the small change in albedo with changes in run-in temperature history.

The *z*-pinch-driven primary in Figure 2 is a 24-mm-diameter, 10-mm-high cylindrical Au hohlraum (24×10-mm^2 notation), with an internal 20-mm-diameter wire array consisting of 300 equally spaced 11.5-μm-diameter tungsten wires. This model shows good consistency between the experimentally measured peak pinch powers (125 ± 25 TW, seven-shot average; Cuneo *et al.*, 2001) and hohlraum radiation temperatures 1.5 ns prior to peak temperature (135 ± 7 eV, two-shot average; Porter, 1997; Baker *et al.*, 1999), in Figure 7. The peak radiation temperature is about 4% higher (140 ± 7 eV). The temperatures are plotted as hundreds of electron volts (i.e., $1 = 100$ eV). We measure the wall re-emission temperatures and albedo-correct upwards to the incident or radiation temperatures for these comparisons (about a 5% correction in this case). The uncertainty associated with the unknown AK gap closure is about 15% in pinch flux. This range is illustrated in Figure 7 by a model assuming 1.5 mm of AK gap closure by the Au hohlraum wall, out of an initial 2 mm, taken from a 2-D RMHD simulation. The pinch power must be assessed more precisely than the current $\pm 20\%$ to affirm the amount of AK gap closure by this global energetics method. A power law scaling relating pinch power and hohlraum temperature is shown on Figure 7 (and on Figs. 10, 11, and 12) and will be discussed in the conclusions. The primary-only configuration will be used to study a number of issues listed in Table 1 such as pinch physics and the scaling of pinch X-ray output

https://doi.org/10.1017/S0263034601193055 Published online by Cambridge University Press

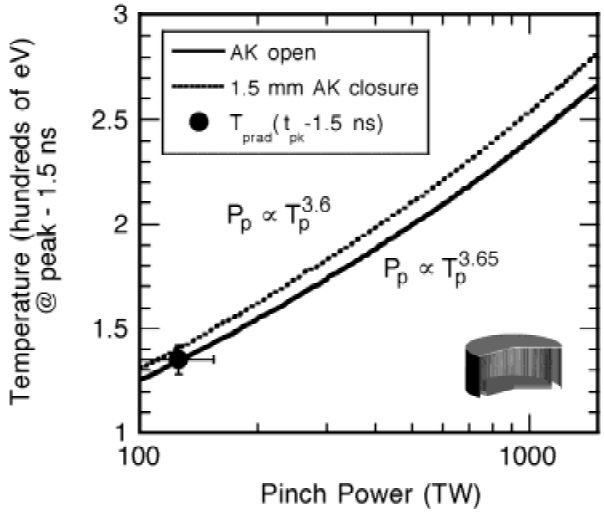

Fig. 7. Comparison of 0-D temperature scaling model for the primary radiation temperature (1.5 ns prior to peak temperature; Fig. 2) compared with measured primary temperature and pinch power, with the 2-mm AK gap fully open (solid line), and closed by 1.5 mm of Au wall material (dotted line).

(see Appendix A), scaling of radiation-driven, magnetically tamped AK gap closure (see Appendix B), and pulse shaping performance. We will also assess pinch power reproducibility which is related to pinch power balance in a double-sided system.

3.2. Primary/secondary configurations

In the case of configurations with one or two primaries and a secondary (Figs. 1, 3, and 4), the description is more involved (Rosen, 1995; Lindl, 1995; Hammer, 1999). The power balance for the primary (X-ray source chamber) is given by

pinch power into primary
− net radiation transport from primary to secondary
= wall loss in primary + loss out diagnostic apertures
+ loss out AK gap power feed(s)
+ loss into Be-spoke material

and for the secondary (X-ray sink or capsule chamber)

pinch power into secondary
+ net radiation transport from primary to secondary
= wall loss in secondary + loss out diagnostic apertures
+ loss into Be-spoke material
+ loss into capsule (if present).

These equations are given below. The power balance for each primary is (j = lower only or lower and upper)

$$f_p P_j - f_{ps} f_v A_{psj} \sigma (T_j^4 - T_s^4) = A_{pj} \sigma T_j^4, \tag{2}$$

where f_p is the fraction of pinch power that remains in the primary, f_{ps} is the average transparency of the Be spokes, f_v is a filter transmission fraction, A_{psj} is the entrance area to the secondary, and the effective loss area for the primary A_{pj} is given by

$$A_{pj} = [(1-\alpha_{pj})A_{wj} + A_{hj} + (1-\alpha_g)A_g + (1-\alpha_{gu})A_{gu} + (1-\alpha_{Be})(1-f_{ps})A_{psj}]. \tag{3}$$

There are two new terms in Eq. (3) compared to Eq. (1): loss of radiation through an additional transmission line AK gap connecting lower and upper pinch (as in Fig. 4) and loss into Be spoke material. The terms included in Eq. (3) encompass four cases. There is no power feed connecting the bottom primary to upper primary ($A_{gu} = 0$) in the case of a single primary (Fig. 2). In this case, $A_{psj} = 0$, and $f_p = 1$ recovering Eq. (1). There is no power feed connecting to an upper pinch ($A_{gu} = 0$), for a single-sided secondary (Fig. 3), or a double-feed, double-pinch (Fig. 1). Finally, there is no standard AK gap power feed for the upper primary ($A_g = 0$), for a single-feed, double-pinch case (Fig. 4). The lower primary has both gap loss terms in this case. The effective gap albedos near peak temperature α_g (= 0.34) and α_{gu} (= 0.40) are taken from 3-D viewfactor calculations (Vesey *et al.*, 1998, 1999) and appear to be insensitive to the exact amount of gap closure.

Summing over (one or two) primaries j, the secondary power balance is given as

$$\sum_j [\, f_s f_{ps} f_v P_j + f_{ps} f_v A_{ps} \sigma (T_j^4 - T_s^4)] = A_s \sigma T_s^4 \tag{4a}$$

or, using $P_u = f_u P_l$,

$$f_s f_{ps} f_v P_l (1 + f_u) + \sum_j f_{ps} f_v A_{ps} \sigma (T_j^4 - T_s^4) = A_s \sigma T_s^4, \tag{4b}$$

where f_s is the fraction of pinch power that directly shines into the secondary, f_u is the ratio of the upper pinch to lower pinch power, and the effective loss area for the secondary A_s is given by

$$A_s = \left[(1-\alpha_s)A_{ws} + A_{hs} + (1-\alpha_{Be})(1-f_{ps}) \sum_j A_{psj} + (1-\alpha_c)A_c \right], \tag{5}$$

which includes a capsule loss term. These two or three coupled equations are solved for the primary and secondary temperatures T_{pj} and T_s, with temperature-varying gold wall albedos, by an iterative scheme, which converges quickly. Table 2 summarizes the parameters used in the equations.

https://doi.org/10.1017/S0263034601193055 Published online by Cambridge University Press

Table 2. *Definitions of parameters in hohlraum equation.*

Parameter	Definition
P_p, P_j	Pinch power for lower or upper pinch
T_p, T_j	Primary hohlraum (radiation) temperature for lower or upper primary
T_s	Secondary hohlraum (radiation) temperature
σ	Stefan–Boltzmann constant
A_{pj}	Effective loss area of each primary (cm^2)
A_s	Effective loss area of the secondary (cm^2)
α_p, α_{pj}	Primary wall albedo given by 1-D RMHD calculation
α_s	Secondary wall albedo given by 1-D RMHD calculation
α_g	Effective AK gap power feed albedo near peak temperature (Lightscape 3-D viewfactor calculation, α_g = 0.34 (Vesey *et al.*, 1998))
α_{gu}	Effective albedo for gap feeding upper pinch in double-pinch (at peak temperature) (Lightscape 3-D viewfactor calculation, $\alpha_g = 0.40$ (Vesey *et al.*, 1998))
α_{Be}	Be spoke albedo (1-D RMHD calculation, $\alpha_{Be} = 0.2$)
α_c	Capsule albedo (assume, $\alpha_c \approx 0.3$ (Lindl, 1995))
f_p	Fraction of pinch power that remains in the primary ($= 1 - f_s f_v f_{ps}$)
f_s	Fraction of pinch power that directly shines into the secondary (viewfactor calculations: 5% to 16% depending on shine shield, secondary and pinch (Vesey *et al.*, 1998, 1999))
f_{ps}	Transparency of the Be spokes (prediction of 2-D RMHD calculation, $f_{ps} = 0.75$ (Hammer *et al.*, 1999))
$\langle f_{ps} \rangle$	Average transparency of both spokes for two-sided systems $= (f_{psl} + f_{psu})/2$
f_v	Correction factor for energy loss in secondary entrance filters ($f_v = 0.9$ for 10 μm parylene filter, 1-D RMHD simulations)
f_u	Ratio of upper pinch power to lower pinch power
f_p, f_s, f_{ps}, f_v	Assumed to be the same for both primaries
A_{psj}	Area of aperture between primary and secondary for each primary (cm^2) can be reduced to account for hohlraum wall motion
$(1 - f_{ps})A_{ps}$	Fraction of area assumed to be filled with Be material (cm^2)
A_{wp}, A_{wj}	Au wall area in each primary (cm^2)
A_{ws}	Au wall area in the secondary (cm^2)
A_{hp}, A_{hj}	Diagnostic aperture area in each primary (cm^2)
A_{hs}	Diagnostic aperture area in secondary (cm^2)
A_g	Area of MITL AK gap (cm^2)
A_{gu}	Area of MITL AK gap feeding upper pinch if present (cm^2)
A_c	Surface area of capsule (if present) (cm^2)

The main power source is the pinch power in the primaries (P_p). Most of the coupling to the secondary is from cavity coupling ($f_{ps} A_{ps}(T_p^4 - T_s^4)$). Some of the pinch power directly shines into the secondary ($f_s f_{ps} P_p$). Both these terms are modified with an average spoke transparency f_{ps}. The radiation coupling from primary to secondary is given by $T_p^4 - T_s^4$ rather than as $\alpha_p T_p^4 - T_s^4$. In the latter case, the first term is the wall re-emission power in the primary ($\alpha_p T_p^4$), rather than the total radiation field (T_p^4, which includes pinch power). This is probably a more appropriate treatment in the case where the direct shine is included separately as in the above equations. However, $T_p^4 - T_s^4$ provides a closer match between the results of the 0-D model and those of 2-D RMHD and viewfactor codes, which show that 70% of the power entering the secondary is from cavity coupling ($f_{ps} A_{ps}(T_p^4 - T_s^4)$) while 30% is from direct pinch shine ($f_s f_{ps} P_p$). The use of $\alpha_p T_p^4 - T_s^4$ gives closer to a 60% cavity coupling/40% direct shine split. The use of T_p^4 may provide a closer approximation to the actual primary radiation field since more than 85% of the pinch power directly heats the primary. This term might also compensate for temperature gradients in the primary (increasing temperature away from the AK gap) which increases radiative power transfer to the secondary.

The largest sources of uncertainty in this model are the actual area of the AK gaps (A_g, A_{gu}) and the value of the direct shine fraction f_s. AK gap closure by the Au hohlraum wall material (see Appendix B) would make the hohlraum a better radiation trap and require lower X-ray power for consistency with the measured wall temperatures. The size of the AK gap near peak temperature is unknown. Two-dimensional RMHD hohlraum simulations (Hammer *et al.*, 1999) indicate about 1.5-mm expansion of the Au wall into the 2-mm gap at peak temperature. Two-dimensional RMHD simulations of pinches have suggested that there may be some current loss at this AK gap based on comparisons to measured X-ray powers (Peterson *et al.*, 1999). There is also indirect evidence for AK gap closure (Cuneo *et al.*, 2001). The direct shine fraction, f_s, is calculated with a viewfactor treatment (Vesey *et al.*, 1998, 1999). These calculations give a range of 5% to 16% for various shine shield, secondary, and pinch diameters, and pinch X-ray angular distributions. Direct shine is reduced for larger shields, smaller secondaries, and for non-Lambertian pinch X-ray emission.

3.3. Example calculations for single-sided secondary configuration

In the case of a single-sided secondary, Eqs. (2) through (5) allow the pinch power and spoke transparency to be treated as two unknowns, and determined from simultaneous measurements of primary and secondary radiation temperature. To illustrate this, we solve Eqs. (2) through (5) for f_{ps}, neglecting the Be-loss terms (depending on f_{ps}) within A_p and A_s. The result in Eq. (6) depends approximately linearly on $\xi = \alpha_s T_s^4 / \alpha_p T_p^4$, the ratio of the wall re-emission flux in the secondary to the wall re-remission flux in the primary:

$$f_{ps} = \frac{\dfrac{\alpha_p}{\alpha_s} A_s}{f_s f_v \left[A_p + \dfrac{\alpha_p}{\alpha_s} A_s \xi \right] + f_v A_{ps} \left[1 - \dfrac{\alpha_p}{\alpha_s} \xi \right]} \xi. \qquad (6)$$

Experiments determine both $\alpha_s T_s^4$ and $\alpha_p T_p^4$ independently, with two, cross-calibrated wall re-emission measurements. ξ can be experimentally determined within $\pm 10\%$ by a relative calibration of two sets of instruments. There is a weak

https://doi.org/10.1017/S0263034601193055 Published online by Cambridge University Press

dependence of Eq. (6) on the temperature (and therefore pinch power) through albedos α_s and α_p, and the effective wall areas A_p and A_s which contain albedos. Physically, Eq. (6) is linear because T_s^4 scales linearly with f_{ps} [Eqs. (2) and (4)], and the variation in T_p is very flat with f_{ps} (see Fig. 9).

Equation (6) is presented primarily to motivate the linear scaling with ξ. Calculations of the Be spoke transparency f_{ps}, including the Be-loss and the variation of albedo with temperature are shown in Figure 8 for a range of pinch powers (110 ± 22 TW), and a range of direct shine fractions (6–16%). Small deviations from linear behavior are indicated. This technique is a feasible indirect inference of f_{ps} because of the insensitivity to the pinch X-ray power shown in Figure 8. Data for the ratio of secondary to primary wall re-emission powers (average of two shots: $\xi = (86.4/112.0)^4 = 0.354 \pm 0.04$) is plotted in Figure 8, indicating an average spoke transparency of 73 ± 7%. This transparency is in good agreement with that inferred from 2-D RMHD simulations of the primary and secondary hohlraum temperatures (Cuneo *et al.*, 2001). Direct 2-D RMHD simulations of the Be spoke transparency including the effects of ablation of spoke material by radiation and current drive predict a 75% transparency and are also in good agreement (Cuneo *et al.*, 2001). There is a stronger dependence of f_{ps} on the direct shine fraction f_s than on pinch power, as shown in Figure 8, hence the importance of including this effect for an inference of transparency. Without direct shine, the inferred spoke transparency could increase by up to 30%. Finally, the entrance area coupling primary to secondary, A_{ps}, is reduced in the experiments from the initial area by the expansion of the Au hohlraum walls (0.3 mm to 0.5 mm from 1-D RMHD simulations). Accounting for the reduction of A_{ps} in the model (as in the above example) increases the net transparency of the Be spokes by about 10%.

Equations (2) and (4) can be added to obtain the pinch power as

$$P_p = \left[A_p + \frac{\alpha_p}{\alpha_s} A_s \xi \right] \sigma T_p^4 \qquad (7)$$

using $f_p + f_s f_v f_{ps} = 1$ from conservation of energy. Equation (7) shows that the pinch power is a weak function of the secondary temperature through the albedos and ξ. Figure 9 plots the primary and secondary radiation temperatures *versus* Be spoke transparency fraction f_{ps}, for a range of pinch powers, and compares them with experimental data. The data are plotted at the transparency independently determined from the analysis in Figure 8. These data (average of two shots) are consistent with a pinch X-ray power of 110 ± 22 TW.

Figure 10 shows the power scaling of hohlraum temperature for the single-sided secondary configuration. This model shows good consistency between the experimentally measured peak pinch powers (100 ± 20 TW, five-shot average) and the primary (118 ± 6 eV, two-shot average) and secondary hohlraum radiation temperatures (93 ± 5 eV, two-shot average), 1.5 ns prior to peak temperature (Cuneo *et al.*,

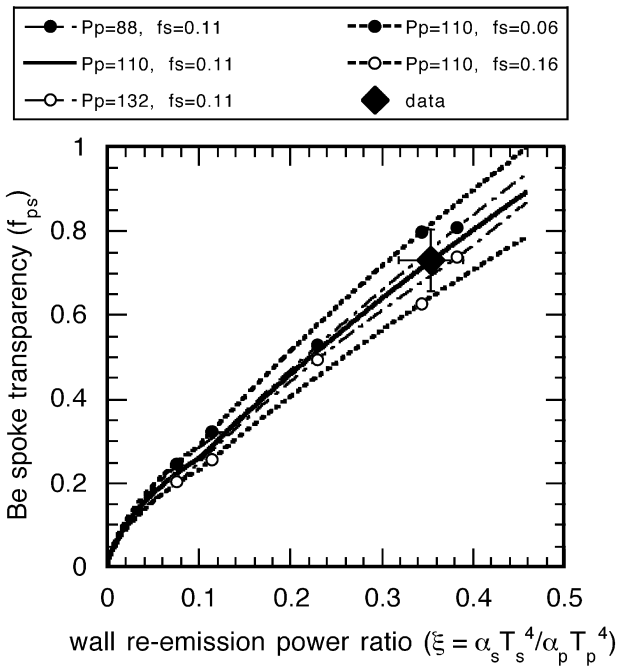

Fig. 8. Calculated Be spoke transparency f_{ps} *versus* the ratio of secondary to primary wall re-emission powers, $\xi = \alpha_s T_s^4/\alpha_p T_p^4$, for a single-sided secondary configuration (Fig. 3). These are shown for a range of pinch powers (110 ± 22 TW, light broken lines with circular symbols), and for a range of direct shine fractions (6% to 16%, heavy dotted lines with circular symbols). The inferred transparency is insensitive to the range of pinch powers. A ±10% uncertainty in transparency results from the range in direct shine fractions and uncertainty in ξ.

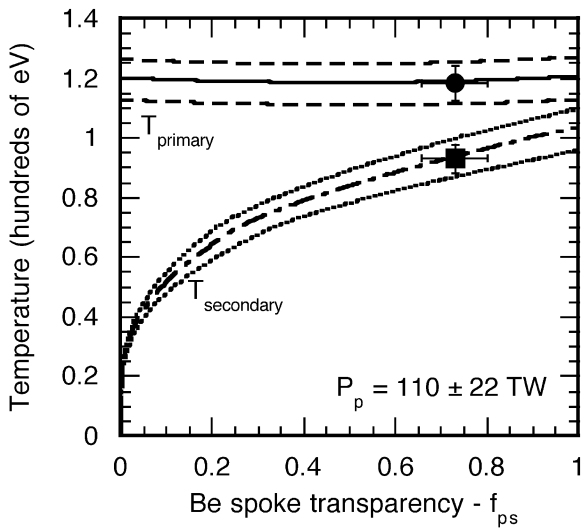

Fig. 9. Primary and secondary temperatures *versus* Be spoke transparency f_{ps} for a single-sided secondary temperature configuration (Fig. 3). These curves are calculated for $P_p = 110 \pm 22$ TW, and for $f_s = 0.11$ with AK gap fully open.

https://doi.org/10.1017/S0263034601193055 Published online by Cambridge University Press

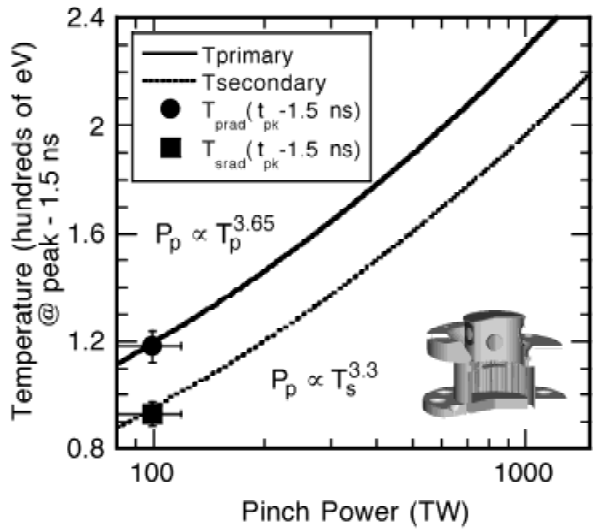

Fig. 10. Comparison of 0-D temperature scaling model for single-sided secondary configuration (Fig. 3) with the measured primary (circle) and secondary (square) radiation temperatures and pinch powers. These curves are calculated for $f_{ps} = 0.70$, and $f_s = 0.11$, with the secondary entrance partially closed (see text) and the AK gap fully open.

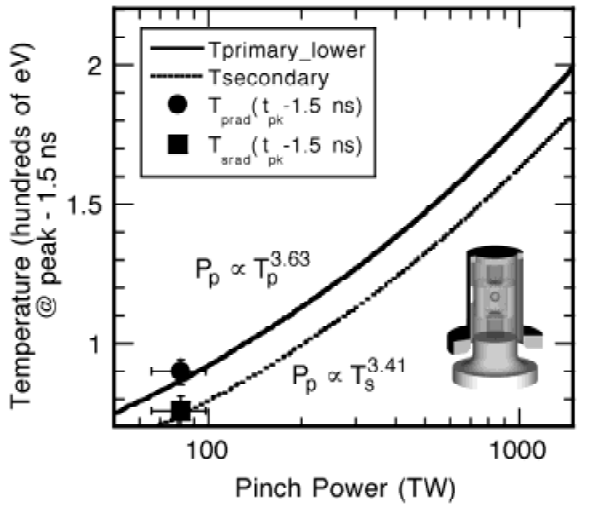

Fig. 11. Comparison of 0-D temperature scaling model for single-sided power feed, double-sided secondary configuration (Fig. 4) with the measured primary (circle) and secondary (square) radiation temperatures and total pinch powers. These curves are calculated for $\langle f_{ps} \rangle = 0.65$, $f_u = 1.0$, and $f_s = 0.11$, with the secondary entrance and AK gaps partially closed. The upper primary temperature is not shown.

2001). The peak temperatures are about 2 to 3% higher than this curve. A model with the AK gap fully open is shown. A case with AK gap partially closed is also within the experimental errors. This primary-secondary configuration can be used to study the scaling of Be spoke transparency with pinch mass and hohlraum temperatures, to study MHD coupling to the secondary and other sources of capsule preheat, and to study azimuthal drive symmetry in the secondary.

3.4. Double-sided secondary configurations

Application of this model to multiple primary systems requires at least one additional measurement, and additional assumptions. There are three equations and seven unknowns. The seven unknowns are three temperatures, two pinch powers, and two spoke transparencies. Any four of the three temperatures and two powers need to be measured to close the set of equations. It is also possible to assume an average spoke transparency for the top and bottom spokes, $\langle f_{ps} \rangle = (f_{pu} + f_{pl})/2$. In this case we must measure any three of the three temperatures and two powers to close the set of equations.

This model is applied to a single-sided power feed, double-sided secondary configuration in Figure 11. In this configuration, a 15-mm-long secondary is positioned within the middle of a 35-mm-long, 20-mm-diameter wire array, creating two separate arrays above and below the secondary. The upper pinch is driven by a transmission-line vacuum feed extended along the outside of the secondary. We measure T_{pl}, T_s, and $f_u = P_{pu}/P_{pl}$, and solve for pinch powers and $\langle f_{ps} \rangle$. Good agreement is observed with the primary (90 ± 5 eV, two-shot average) and secondary (76 ± 5 eV, two-shot average) radiation temperatures 1.5 ns prior to peak temperature at the observed total pinch power of 82 ± 16 TW (two-shot average; Cuneo *et al.*, 2000, 2001). Greater load inductance in this configuration resulted in lower total load current and pinch power. Greater wall area (two primaries, transmission line feed coupling the two primaries, and a larger secondary), additional radiation loss pathways (e.g., the upper AK gap), and lower pinch power results in lower secondary temperature. The upper primary has smaller radiation loss than the lower primary since it has only one AK gap. Temperatures for the upper and lower primary are equal for $f_u = P_u/P_l = 0.8$. A single-sided current feed does not scale to meet high-yield requirements of more than 210 eV (Hammer *et al.*, 1999) in the secondary at 63 MA. However, this configuration can be used to study pinch power balance, simultaneity, and polar radiation symmetry, and possibly perform capsule implosions, prior to the development of a machine architecture compatible with a two-sided power feed (Struve *et al.*, 1999).

Figure 12 gives results for the high-yield configuration of Figure 1 (a double-sided power feed, double-sided secondary), with and without AK gap closure by the Au wall material, showing the range of uncertainty from this effect. The upper lines for the primary and secondary are the cases with AK gap closure. The closure was assumed to be 1.5 mm out of an initial 2 mm. The single-sided Z secondary data from Figure 10 is scaled up by $2^{1/4}$ to 111 ± 6 eV to approximately account for the temperature increase from an additional primary. The results in Figures 7, 10, 11, and 12 indicate that the hohlraum energetics and radiation coupling (Cuneo *et al.*, 1999*a*, 1999*b*, 2000, 2001) scale to the high-yield requirements of more than 210-eV secondary-wall re-

https://doi.org/10.1017/S0263034601193055 Published online by Cambridge University Press

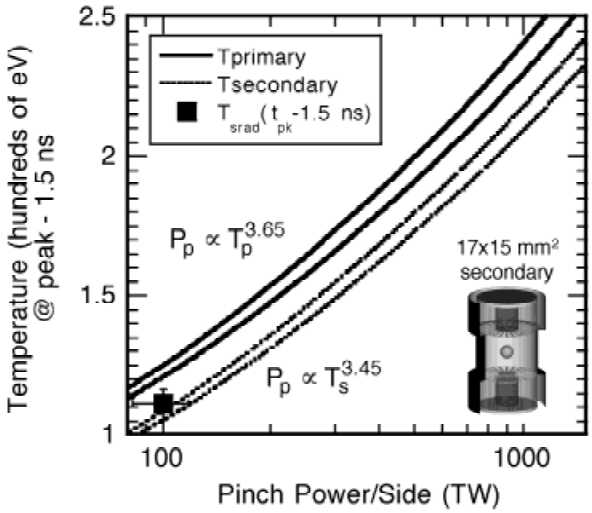

Fig. 12. Comparison of 0-D temperature scaling model for double-sided power feed, double-sided secondary configuration (Fig. 1) and comparison with scaled Z secondary radiation temperature data. Note that the power axis is power/side not total power. The primaries are 24×10 mm^2 with a single aperture. The secondary is a 17×15 mm^2. The single-sided Z secondary data from Figure 10 is scaled up by $2^{1/4}$ to approximately account for the temperature increase from an additional primary. These curves are calculated for $\langle f_{ps} \rangle = 0.75$, $f_u = 1.0$, and $f_s = 0.11$. The upper curves for the primary and secondary assume 1.5 mm of AK gap closure out of the initial 2 mm. The lower curves assume no AK gap closure. The upper and lower primary temperatures are the same for this case with $f_u = 1.0$.

emission temperature. A pinch power per side of ≥940 TW/side (with AK closure) and ≥1100 TW/side (with no AK closure) is required for the case in Figure 12 with a 17×15 mm^2 secondary. The use of Au-Gd hohlraum cocktail walls (Hammer *et al.*, 1999) would lower the pinch power requirements by about 10% or increase the secondary temperatures by about 3% at fixed power, because of the increase in Au/Gd wall opacity by 50% compared to Au (Orzechowski *et al.*, 1996).

4. CONCLUSIONS AND SUMMARY OF SCALING MODELS

These 0-D models show good agreement with the measured pinch X-ray powers and hohlraum wall temperatures to within ±20% in flux (±5% in temperature) accounting for uncertainties in aperture closure and instrumental calibration for all three geometries in Figures 2–4. Issues such as partial AK gap closure, and non-Lambertian pinch emission affect the agreement to about the ±20% level in X-ray flux. This is within the experimental uncertainty, hence we cannot conclude anything about these issues from this model and these data. This level of flux uncertainty is about the best currently possible for measurements of wall re-emission, and pinch powers, and is typical also for laser hohlraum measurements (Lindl, 1995). Improvements in temperature or pinch measurement accuracy or direct measurements of AK gap closure or pinch angular emission profile are necessary to improve energetics assessment beyond the ±20% level.

Previous analytic work for laser-driven hohlraums shows that the Au wall loss energy is proportional to $(1 - \alpha_p)T^4$ which scales as $T^{3.4}$ for the STA opacity table (Lindl, 1995; Rosen, 1995, 1996). An abbreviated power balance description could balance input power against strictly wall loss (i.e., $P_p \propto T^{3.4}$), since wall loss dominates the hohlraum loss. A power law fit to the primary temperatures given in Figures 7, 10, 11, and 12 shows that

$$P_p \propto T_p^n, \tag{8}$$

where the exponent n of temperature varies from 3.6 to 3.65. The different exponent of temperature in the scaling of wall loss between this and the previous analytic work results because of the different temperature pulse shape for the *z*-pinch-driven hohlraums compared to those for laser hohlraums, as well as from additional loss out the AK gap and into Be spoke material. Power law fits to the secondary temperatures given in Figures 10, 11, and 12 show that

$$P_p \propto T_s^m, \tag{9}$$

where m varies from 3.3 to 3.45. The reduction in exponent results because of the radiative coupling between primary and secondary. This can be easily shown by an approximate solution of Eqs. (2) through (5) where only source, wall loss, and radiative coupling terms are kept (Rosen, 1995), and direct shine, AK gap, aperture, Be, and capsule loss terms are neglected. This analytic solution indicates that the exponent $m = n^2/4$ (e.g., $3.3 \approx 3.65^2/4$ in Fig. 10), which is close to the observed scaling of the secondary temperature curves. We have high confidence in these models since they are based on a large amount of work on the diffusive loss of X rays into Au walls done with laser-driven hohlraums (Lindl, 1995; Rosen, 1996).

There are other issues that could affect the scaling of hohlraum temperatures with higher current *z*-pinch drivers as shown in Figures 7, 10, 11, and 12. For example, the *z*-pinch mass must increase with the square of the pinch current for a constant implosion time. Hence a pinch at 60 MA must have nine times the mass as at 20 MA. The total energy (kinetic + magnetic + ohmic) available to be radiated by the pinch scales as the square of the driver current. Experimentally, pinch X-ray energy has been observed to scale with the square of the driver current between 1 MA and 20 MA (Matzen, 1997; Spielman *et al.*, 1998). The increasing pinch opacity and mass (Hammer *et al.*, 1999) will decrease the net radiated X-ray power below the I^2 scaling of total energy because of energy tied-up in the pinch heat capacity on the time scale of the power pulse. 0-D and 2D scaling models for the level of pinch current and mass where tungsten pinch opacity limits X-ray power are given in Appendix A. Whereas the total energy scales as I^2, we find that the internal energy of the pinch scales as $I^{2.41}$ to $I^{2.82}$. This

https://doi.org/10.1017/S0263034601193055 Published online by Cambridge University Press

implies that an increasingly larger fraction of the total energy must go into heat capacity as the pinch mass and opacity increase. The net radiated energy of a tungsten pinch from this simple model is observed to scale as $I^{1.71}$ to $I^{1.84}$ over the range from 20 to 65 MA. Zero-dimensional and 2-D RMHD models discussed in Appendix A place bounds on radiated pinch energies between 6.2 and 9.3 MJ at 62 MA. Assuming that 6 ns to 7 ns pulse widths can be attained at 62 MA as on Z, X-ray powers of 950 TW to 1430 TW would be attained, bounding what is required for the current high-yield capsule design.

The electromagnetic power that supplies current to the pinch is delivered through a 2-mm AK gap at the base of the pinch. This gap is subjected to radiation fields of 250 eV in the primary (Fig. 12), at peak magnetic fields of more than 1000 T in the high yield scale system. A simple analytic scaling for magnetically tamped, radiation-driven AK gap closure is given in Appendix B to provide some guidance on this issue. We find that on Z, the magnetic pressure exceeds the radiation ablation pressure on the Au wall by a factor of 2 to 4 during the first 90 ns of the implosion. This may explain why these small AK gaps are able to deliver current during the 100-ns pinch implosion time, even as the transmission line surfaces are bathed in radiation at more than 30 eV. We find that the ratio of magnetic pressure to radiation ablation pressure scales as $I^{0.56}$, indicating favorable scaling on larger drivers. The reasonably well-behaved AK gap we observe on Z (Cuneo *et al.*, 2001) may imply a well-behaved AK gap on higher current drivers.

Future work will explore the pinch opacity and AK gap closure issues experimentally (W.A. Stygar, pers. comm.). These and the other issues listed in Table 1 are part of our ongoing high-yield assessment for *z* pinches.

ACKNOWLEDGMENTS

We gratefully acknowledge the experimental efforts of the Z operations teams led by J. Seamen, including the wire array lab (T.L. Gilliland, P.G. Reynolds), target development lab (D. Hebron, S. Dropinski, R. Hawn), and materials processing and coating lab (J. McKenney). We also thank the following for development and fielding of various diagnostics: D.F. Wenger, H. Seamen, and P. Primm for the transmission grating spectrometers and pinhole cameras, G.A. Chandler, J. Torres, and J. McGurn for XRDs and bolometers, and W.A. Stygar and T. Wagoner for B-dot loop current measurements. We thank K. Cochrane for the power law fit to the Sesame Equation of State for tungsten in Eq. (A4). We acknowledge helpful conversations with D.L. Peterson, W.A. Stygar, R.E. Chrien, and R.B. Spielman. We thank M.K. Matzen and J.P. Quintenz for programmatic support. Sandia is a multiprogram laboratory operated by Sandia Corporation, a Lockheed Martin Company, for the U.S. Department of Energy under Contract No. DE-AC04-94AL85000.

REFERENCES

Bar-Shalom, A. *et al.* (1989). *Phys. Rev. A* **40**, 3183.
Baker, K.L. *et al.* (1999). *Appl. Phys. Lett.* **75**, 775.
Baker, K.L. *et al.* (2000). *Phys. Plasmas* **7**, 681.
Chandler, G.A. *et al.* (1999). *Rev. Sci. Instrum.* **70**, 561.
Chrien, R.E. *et al.* (1999). *Rev. Sci. Instrum.* **70**, 557.
Cuneo, M.E. (1999). *IEEE Trans. Dielectrics and Electrical Insulation* **6**, 469.
Cuneo, M.E. *et al.* (1999*a*). *26th IEEE Conf. on Plasma Sci.*, Monterey, CA (IEEE, Piscataway, NJ).
Cuneo, M.E. *et al.* (1999*b*). *Bull. Am. Phys. Soc.* **44**, 40.
Cuneo, M.E. *et al.* (2000). *27th IEEE Conf. on Plasma Sci.*, New Orleans, LA (IEEE, Piscataway, NJ).
Cuneo, M.E. *et al.* (2001). *Phys. Plasmas* **5**, 2257.
Deeney, C. *et al.* (1997). *Phys. Rev. E* **56**, 5945.
Hammer, J.H. *et al.* (1999). *Phys. Plasmas* **6**, 2129.
Holian, K.S. (1984). *LA-10160-MS UC-34*, Los Alamos, NM: Los Alamos National Laboratory.
Lash, J.S. *et al.* (2000). In *Inter. Fusion Science and Applications 99* (Labaune, C., Hogan, W.J., and Tanaka, K.A., eds.), p. 583. Paris: Elsevier.
Leeper, R.J. *et al.* (1999). *Nucl. Fusion* **39**, 1283.
Lindl, J.D. (1995). *Phys. Plasmas* **2**, 3933.
Matzen, M.K. *et al.* (1997). *Phys. Plasmas* **4**, 1519.
Matzen, M.K. *et al.* (1999). *Plasma Phys. Control. Fusion* **41**, A175.
Nash, T.J. *et al.* (1999). *Phys. Plasmas* **6**, 2023.
Olson, R.E. *et al.* (1999). *Fusion Technol.* **35**, 260.
Orzechowski, T.J. *et al.* (1996). *Phys. Rev. Lett.* **77**, 3545.
Peterson, D.L. *et al.* (1998). *Phys. Plasmas* **5**, 3302.
Peterson, D.L. *et al.* (1999). *Phys. Plasmas* **6**, 2178.
Porter, J.L., Jr. (1997). *Bull. Am. Phys. Soc.* **42**, 1948.
Rosen, M.D. (1995). *UCRL-JC-121585*, Livermore, CA: Lawrence Livermore National Laboratory.
Rosen, M.D. (1996). *Phys. Plasmas* **3**, 1803.
Rosen, M.D. (1999). *Phys. Plasmas* **6**, 1690.
Ruggles, L.E. *et al.* (2001) *Rev. Sci. Instrum.* **72**, 1218.
Sanford, T.W.L. *et al.* (1996). *Phys. Rev. Lett.* **77**, 5063.
Sanford, T.W.L. *et al.* (1999). *Phys. Rev. Lett.* **83**, 5511.
Sanford, T.W.L. *et al.* (2000). *Phys. Plasmas* **7**, 4669.
Slutz, S.A. *et al.* (2001). *Phys. Plasmas* **8**, 1673.
Spielman, R.B. *et al.* (1998). *Phys. Plasmas* **5**, 2105.
Spielman, R.B. *et al.* (1999). *Rev. Sci. Inst.* **70**, 651.
Stygar, W.A. *et al.* (1997). In *Proc. of the Int. Pulsed Power Conf.* (Cooperstein, G. and Vitkovitsky, I., Eds.), Vol. 2, p. 1258. Piscataway, NJ: IEEE.
Stygar, W.A. *et al.* (2001). *Phys. Rev. E* **64** (in press).
Struve, K.W. *et al.* (1999). In *Proc. of the Int. Pulsed Power Conf.* (Stallings, C., and Kirbie, H., Eds.), Vol. 1, p. 493. Piscataway, NJ: IEEE.
Vesey, R.A. *et al.* (1998). *Bull. Am. Phys. Soc.* **43**, 1903.
Vesey, R.A. *et al.* (1999). *Bull. Am. Phys. Soc.* **44**, 227.
Zimmerman, G.B. & Kruer, W.L. (1975). *Comments Plasma Phys. Control. Fusion* **2**, 51.

APPENDIX A: SCALING OF PINCH X-RAY OUTPUT WITH PINCH MASS AND CURRENT

The total energy (kinetic + magnetic + ohmic) *available* for conversion into radiation by the *z*-pinch scales with the square of the pinch current. This is simply a statement of conservation of energy. We assume that some fraction of the total available system energy

(here E_{tot}) is partitioned between radiated energy and internal energy tied up in the heat capacity of the material:

$$E_{tot} = E_{rad} + E_{int}. \tag{A1}$$

The second term becomes increasingly important as the pinch mass and opacity increases. We expect $E_{tot} \approx E_{rad}$ at low mass and opacity. The radiated energy has been observed to scale as I^2 on drivers at 1–20 MA (Matzen, 1997).

The measured power on Z is 125 ± 25 TW in a 6.4 ± 0.5-ns FWHM pinch power pulse. This gives an effective energy in the pulse of about 0.8 ± 0.1 MJ at 19-MA load current. The results of this appendix give an internal energy of 0.14 MJ at 6 mg, and 19 MA, hence we assume the total energy scales as

$$E_{tot} = 0.94\left(\frac{I}{19}\right)^2 \text{ MJ}. \tag{A2}$$

A 0-D thin shell implosion model gives 650 kJ of instantaneous kinetic energy evaluated at a 20:1 convergence ratio. At stagnation, this kinetic energy is rapidly thermalized by shock heating and radiated (Peterson *et al.*, 1998, 1999). The effective radiated energy on Z is 23% higher than this kinetic energy at stagnation, with a 2-mm AK gap. This additional energy may result from PdV work done by the magnetic field on the imploding plasma starting just prior to peak radiated power (Peterson *et al.*, 1999). Ohmic energy is a small contribution (6%) to the system energetics for these fast pinches (Peterson *et al.*, 1998, 1999). Two-dimensional RMHD simulations without AK gap loss at the base of the pinch give a radiated energy about 70–80% larger than the kinetic energy at stagnation (Cuneo *et al.*, 2001), about 1100 kJ for this 20-mm-diameter wire array. Including AK gap loss in a 2-D RMHD simulation (Peterson *et al.*, 1999; Cuneo *et al.*, 2001) gives a radiated energy of 850 kJ in close agreement with the Z scaling of Eq. (A2), about a 30% reduction in energy compared to simulations without AK gap loss (Cuneo *et al.*, 2001). Equation (A2) assumes that the energy available to be radiated continues to scale up as 1.23 times the kinetic energy at stagnation as the mass and current are increased. This is a conservative assumption because Appendix B shows that the AK gap performance scales favorably with drive current, and the 2-D simulations show a larger factor (1.7). In addition, somewhat larger AK gaps could be used on higher current drivers.

The 6-mg pinch mass used on the Z arrays will increase with the square of the current to keep implosion time constant,

$$m_p = 6\left(\frac{I}{19}\right)^2 \text{ mg}. \tag{A3}$$

The internal energy or heat capacity of the pinch is given by

$$E_{int} = m_p e_{int} = m_p 4.4 \rho_{\text{g/cm}^3}^{-0.12} T_{\text{heV}}^{1.37} \text{ MJ} \tag{A4a}$$

where e_{int} is the tungsten specific heat, m_p and ρ are the mass and density of the pinch at stagnation, and T is the pinch temperature in hundreds of electron volts. This power law fit to the tungsten pinch-plasma specific heat e_{int} is derived from data in the Sesame Equation of State package (Holian, 1984) over the density and temperature ranges of $0.05 < \rho < 0.2$ g/cm^3, and $0.15 < T < 0.9$ keV. We integrate the heat capacity across the temperature profile of the pinch to obtain the correction factor g [see Eq. (A8)], where e_c is the specific heat evaluated at the core temperature:

$$E_{int} = 2\pi l_p 4.4 \rho^{0.88} \int_0^{r_s} T(r)^{1.37} r\, dr = m_p e_c g, \tag{A4b}$$

where r_s and l_p are radius and length of the pinch at stagnation.

We assume the pinch is a static, uniform mass density cylinder of hot tungsten. We neglect any radial dependence of the source and the internal energy. The Rosseland mean free path is allowed to vary with temperature [Eq. (A7)]. Under these conditions, we obtain a temperature profile from a solution to the 1-D cylindrical radiation heat diffusion equation:

$$T(r) = T_c\left(1 - f\frac{r^2}{r_s^2}\right)^{1/[4(\lambda+1)]}, \tag{A5}$$

where T_c is the pinch core temperature, and where f is a small correction given to first order by

$$f = 1 - \left(\frac{4}{3(\lambda+1)\tau_c}\right)^{\lambda+1}. \tag{A6}$$

Here $\lambda = 1.5/4 = 0.375$ and τ_c is the optical depth evaluated at the core temperature with the full pinch radius. Note that for high optical depth systems, f is near 1, that is, for $\tau_c = 10$, $f = 0.96$. The diffusion approximation is reasonable for $\tau_c \geq 5$. The optical depth τ_c of the W pinch plasma at the core temperature is

$$\tau_c = K_R \rho r_s = 6 \times 10^3 \rho_{\text{g/cm}^3}^{1.3} T_{c(\text{heV})}^{-1.5} r_s, \tag{A7}$$

where we assume that the tungsten plasma Rosseland mean opacity K_R can be approximated by a power law fit to the Rosseland mean opacity of Au given in Lindl (1995). Substituting (A5) into (A4b) and completing the integral, we obtain the correction factor g for internal energy:

$$g = \left[\frac{1 - (1-f)^{(\gamma/(\lambda+1)+1)}}{\left(\frac{\gamma}{\lambda+1}+1\right)f}\right], \tag{A8}$$

where $\gamma = 1.37/4 = 0.34$. This correction factor g is 0.83 at 20 MA, which corresponds to an internal energy evaluated at about 87% of the pinch core temperature.

The radiated energy lost through the outer surface of this optically-thick z-pinch cylinder is given by

$$E_{rad} = \frac{8}{3(\lambda+1)}\sigma T_s^4 A_s t_p = 0.019 A_s T_s^4 t_p \text{ MJ}, \tag{A9}$$

where T_s is defined as the temperature of the surface of the tungsten cylinder, at $r = r_s$ in Eq. (A5). Equation (A9) satisfies the Milne boundary condition at the pinch edge. Radiation is collected from a depth of order a mean free path $(K_R\rho)^{-1}$, looking into the pinch with a temperature profile given by (A5), where A_s, and T_s are the pinch surface area and surface temperature respectively in centimeters squared and hectoelectron volts, and t_p is the pinch power pulse FWHM in nanoseconds.

https://doi.org/10.1017/S0263034601193055 Published online by Cambridge University Press

Given the scaling of m_p (and ρ) with I^2, and assuming that T_s^4 scales roughly with I^2, we find that the internal energy E_{int} scales as $I^{3.1}$ from Eqs. (A4), (A5), and (A7). This implies that an increasingly larger fraction of the total energy (which scales as I^2) must go into heat capacity as the pinch mass and opacity increase. Equations (A1) through (A9) are iterated to find a self-consistent combination of E_{rad}, E_{int}, T_c, T_s, τ_c consistent with the total energy in Eq. (A2). Note that the only current scaling assumptions that are input into the model are that E_{tot} and ρ scale with I^2 [Eq. (A2), and (A3)]. Figure 13 shows results from this 0-D model (heavy and light lines) for a case with $r_s = 0.1$ cm, and $l_p = 1.0$ cm. The light solid lines give a 0-D model case with the optical depth reduced by a factor of 5 from Eq. (A7) to study the sensitivity of internal energy to optical depth. The Z scaling data (solid circle) and results from 2-D RMHD tungsten pinch simulations including the effect of the Rayleigh–Taylor (RT) instability (open symbols) are also shown in Figure 13.

Power law fits to the 0-D curves in Figure 13 show that the internal energy scales as $I^{2.82}$ from 20–65 MA. About 62% of the energy goes into radiation (6.2 MJ) and 38% into pinch heat capacity (3.8 MJ) at 62 MA. The internal energy is only about 15% of the total energy at 19 MA pinch current (136 kJ). The net radiated energy ($= E_{tot} - E_{int}$) scales as $I^{1.71}$ over the range from 20 to 65 MA. There is a clear change in scaling compared to the historical observation of $E_{tot} \propto E_{rad} \propto I^2$ on 1–20-MA drivers (Matzen, 1997; Spielman *et al.*, 1998). The Rosseland optical depth of the core scales as $I^{1.4}$ from about 11.6 at 19 MA to 62.4 at 62 MA. The surface temperature T_s scales as $I^{0.43}$ from about 178 eV at 19 MA to 296 eV at 62 MA. The core temperature T_c scales as $I^{0.79}$ from 331 eV at 19 MA to 840 eV at 62 MA.

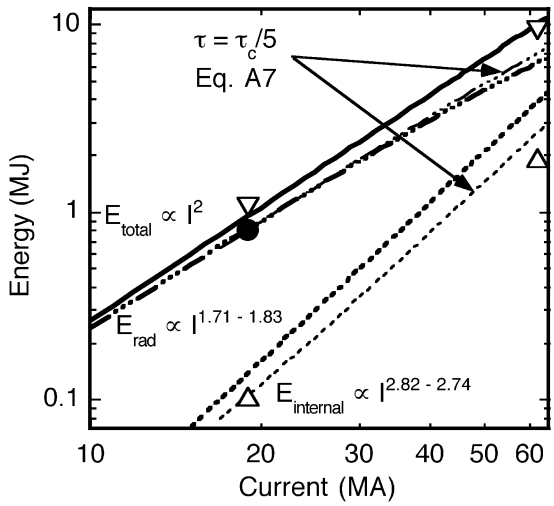

Fig. 13. 0-D partition of total energy (solid line) between radiated (broken line) and internal energy (dashed lines) as a function of pinch current for a static, uniform density W pinch column with constant implosion time. The light lines are the internal and radiated energies with an optical depth reduced by a factor of 5 from Eq. (A7). The total energy was normalized to the measured Z data (0.8-MJ radiated) and 0.14 MJ internal (estimate) at 19-MA load current, shown as a solid circle. The first number in the given range of power law scaling corresponds to the larger optical depth. The open symbols show radiated (inverted triangles) and internal (triangles) energy predictions from 2-D RMHD simulations with a random density perturbation to simulate the growth of the Rayleigh–Taylor instability. The 2-D simulations use a scaling close to that of Eq. (A3): a 5.5-mg load at 19 MA and a 50-mg load at 62 MA.

The RT instability growth is expected to dominate the pinch FWHM (Spielman *et al.*, 1998) based on 2-D RMHD simulations (Peterson *et al.*, 1998, 1999; Hammer *et al.*, 1999). These simulations approximate the implosion of the wire array as that of a 2-D shell. Random density perturbations are used as a seed to initiate the growth of RT. 2-D RMHD simulation results for radiated energy (inverted triangles) and internal energy (triangles) are shown in Figure 13 at 19 and 62 MA. The mass of these arrays is approximately that given by Eq. (A3). The array at 19 MA used 5.5 mg, while that at 62 MA used 50 mg. The effect of the RT instability will reduce the effective optical depth of the *z* pinch below that from Eq. (A7) because of the breakup of the ideal cylinder into an RT bubble–spike structure (Slutz *et al.*, 2001). Figure 13 also shows 0-D model results from a reduction of the optical depth of Eq. (A7) by an arbitrary factor of 5 (light lines) to account for the effects of the instability on the ideal cylindrical solution. Slutz derived a factor of 2.7 reduction (Slutz *et al.*, 2001) from an analytic RT model. In addition to RT, turbulent mixing of the core and outer layers could also bring hot material to the surface and increase radiated energy (Hammer *et al.*, 1999). The effective Rosseland optical depth of the 0-D model now scales from 3.6 at 19 MA to 18.7 at 62 MA. With the reduced optical depth, about 72% of the total energy is radiated (7.0 MJ) and 28% (2.7 MJ) is trapped in heat capacity at 62 MA. At 19 MA, 106 kJ (10%) is trapped in heat capacity. The internal energy in the 2-D RMHD simulations increases from 112 kJ at 19 MA to 1.94 MJ at 62 MA, scaling as $I^{2.41}$. These are in reasonable agreement with the 0-D model values with reduced optical depth. However, the radiated energy predicted by the 2-D RMHD simulation exceeds the 0-D model and the Z normalization point by about 33%, increasing from 1.06 MJ at 19 MA to 9.3 MJ at 62 MA with tungsten, scaling as $I^{1.84}$. The scaling of radiated energy and the energy budget in 2-D simulations requires further study, but we believe the larger energy results because the 2-D simulations in Figure 13 do not include AK gap current loss as discussed previously (Cuneo *et al.*, 2001).

Note that the internal energy increases from 9% of the total at 19 MA to 17% of the total at 62 MA, in the 2-D model. This is below the fraction predicted by the 0-D model of 28 to 38% at 62 MA. A principal conclusion of these models is that the internal energy does not dominate the total energy budget of a 60-MA *z* pinch. The internal energy may be bound between 15% and 30% of the total energy (internal + radiated) at 62 MA according to these models. The internal energy is equal to the radiated energy at currents exceeding 90 MA, according to the 0-D model.

If the wire array pinch can be modeled as the implosion of a 2-D MHD shell, perhaps the radiated energies of a 3-D pinch at high-yield scale may be bound by the 0-D values (from scaled Z data) and the 2-D values (without AK gap loss), between 6.2 MJ and 9.3 MJ at 62 MA. The linear growth time for RT on a shell scales with $(\text{acceleration})^{0.5} \times$ time; hence a system with a fixed size, force/mass, and implosion time might be expected to have the same pinch radiation FWHM that we observe on Z of 6 ns to 7 ns. This implies an X-ray power of 950 TW to 1430 TW at 62 MA with 6.2 MJ to 9.3 MJ radiated in 6.5 ns, bounding what is required for the current high-yield capsule design. Pinch opacity could broaden the pulse. Low-*Z* pinch materials were used in Hammer *et al.* (1999) to decrease the optical depth in 2-D RMHD simulations and resulted in 1200 TW (8.4 MJ in 7 ns) at 63 MA. The pulse width and total energy for wire array implosions may not scale as ex-

https://doi.org/10.1017/S0263034601193055 Published online by Cambridge University Press

pected for a 2-D shell with R-T. The scaling of wire ablation rate, precursor formation and other issues may have an important effect on the scaling of pulse width and energy with current. Experiments that measure the mass distribution of wire-array *z* pinches, and study the scaling of radiated power from wire arrays with increasing mass and current will be critical.

APPENDIX B: SCALING RADIATION ABLATION AND MAGNETIC TAMPING PRESSURES

The size of the anode-cathode (AK) gap power feed at the time of peak hohlraum temperature is unknown and remains an uncertainty in our modeling of the energetics (see Figs. 7 and 12). AK gaps have been operated as small as 1.5 mm on the Z accelerator at 19-MA peak current on a 1-cm radius (Porter, 1997). An important question is how the AK gap performance will scale at higher hohlraum temperatures (250 eV) and higher magnetic fields (1200 T at 60 MA and 1-cm radius). As noted above, 2-D RMHD simulations of hohlraums (Hammer *et al.*, 1999) and pinches (Peterson *et al.*, 1999) and experiments (Cuneo *et al.*, 2001; W.A. Stygar, pers. comm.) indirectly show some closure of this AK gap. AK gap closure by the Au hohlraum wall material would make the hohlraum a better radiation trap. Closure of the AK gap however, could result in electron loss that would decrease the pinch X-ray output. Further experiments are required to elucidate this balance, and its scaling with gap size, hohlraum temperature, wall material, and current. This appendix provides a simple comparison of radiation ablation pressure to magnetic pressure as a first step to understanding the behavior of these small, high-energy-density, magnetized AK gaps.

The scaling of radiation ablation pressure can be calculated by equating the absorbed radiation flux intensity to the hydrodynamic power (Lindl, 1995):

$$I = (1-\alpha)\sigma T^4 = \frac{5}{2} P_a U_f \propto \frac{5}{2} P_a C_s \ \mathrm{W/cm^2}, \tag{B1}$$

where α is the albedo of the blow-off material, T is the radiation temperature of the incident radiation, P_a is the radiation ablation pressure on the surface, U_f is the flow velocity of the material, C_s is the isothermal sound speed $= 9.76(ZT_{heV}/\mu)^{1/2}$ cm/μs for T in hundreds of electron volts, and μ is the ion mass in units of proton mass. In the case of a low-Z material with low opacity (high transparency to incident radiation) we find ($Z/\mu = 1/2$ for fully stripped low-Z material):

$$P_{a(low\_Z)} = 4T_{\mathrm{heV}}^{3.5} \ \mathrm{Mbar} \tag{B2}$$

for T in hundreds of electron volts, and $\alpha = 0.3$ appropriate for a low-Z material. The result in (B2) can be scaled to account for the decrease in expansion velocity and increase in albedo of the high-Z Au wall material which will lower the ablation pressure compared to the scaling in B2:

$$P_{a(high\_Z)} = \frac{C_{s(low\_Z)}(1-\alpha)_{high\_Z}}{C_{s(high\_Z)}(1-\alpha)_{low\_Z}} P_{a(low\_Z)}. \tag{B3}$$

The ratio of sound speeds is

$$\frac{C_{s(low\_Z)}}{C_{s(high\_Z)}} = 2.1T_{\mathrm{heV}}^{-0.225} \tag{B4}$$

for T in hundreds of electron volts, using a result for the average ionization state of Au as a function of temperature from Lindl (1995):

$$\bar{Z} = 23T_{\mathrm{heV}}^{0.45}. \tag{B5}$$

Combining Eqs. (B2), (B3), and (B4), we find

$$P_{a(high\_Z)} = 12T_{\mathrm{heV}}^{3.275}(1-\alpha)_{high\_Z} \ \mathrm{Mbar}. \tag{B6}$$

The Au wall loss fraction $(1-\alpha)$ is given approximately by Lindl (1995):

$$(1-\alpha)_{high\_Z} = \frac{0.32}{T_{\mathrm{heV}}^{0.7}\tau_{\mathrm{ns}}^{0.38}}, \tag{B7}$$

where T is in hundreds of electron volts and τ is the radiation pulse width in nanoseconds. The effective τ for Z parameters at peak temperature based on the 1-D RMHD calculations reported above (Fig. 6) is about 9.4 ns, giving the calculated albedo of 0.89 at 140 eV. Substituting (B7) into (B6) we find

$$P_{a(high\_Z)} = 3.84 \frac{T_{\mathrm{heV}}^{2.6}}{\tau_{\mathrm{ns}}^{0.38}} \ \mathrm{Mbar}. \tag{B8}$$

Equations (B6) and (B8) are in reasonable agreement with 1-D RMHD simulations. The magnetic pressure is given by

$$P_m = \frac{B^2}{8\pi} = 1.57\times10^{-3} \frac{I_{\mathrm{MA}}^2}{r_{\mathrm{cm}}^2} \ \mathrm{Mbar} \tag{B9}$$

where I is the load current in mega-amperes and r is the radius of the AK gap in centimeters. Using Eqs. (B8), (B9) and (8) we find the ratio of magnetic to radiation ablation pressure:

$$\frac{P_m}{P_a} \propto \frac{B^2}{T^{2.6}} \propto \frac{I^2}{T^{2.6}} \propto \frac{T^{3.6}}{I^{1.44}} \propto T \propto I^{0.56}, \tag{B10}$$

which implies that the magnetic tamping scales upwards faster than the radiation ablation pressure. The reasonably well-behaved AK gap we observe on Z (Cuneo *et al.*, 2001) may imply a well-behaved AK gap on higher current drivers. Note also that the scaling of this ratio is far less favorable for low-Z contaminant layers. In this case we find a much weaker scaling with current: $P_m/P_a \propto B^2/T^{3.5} \propto I^{0.1}$, which emphasizes the importance of providing power flow surfaces free of hydrocarbon contamination (Spielman *et al.*, 1998; Cuneo, 1999).

It must also be noted that both the temperature and current vary as a function of time. Figure 14 plots the magnetic pressure [Eq. (B9)] and high-Z Au wall radiation ablation pressure [Eq. (B8)] as a function of time for both Z parameters (20-MA peak load current, ≈140-eV peak radiation temperature) and parameters rel-

https://doi.org/10.1017/S0263034601193055 Published online by Cambridge University Press

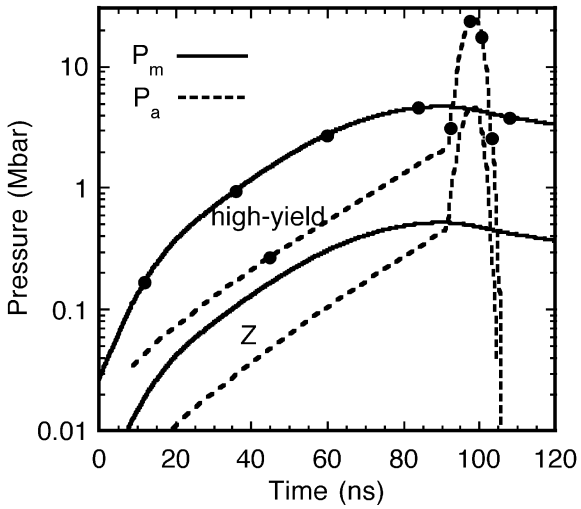

Fig. 14. A plot of magnetic pressure P_m from Eq. (B8) (solid lines) and radiation ablation pressure P_a from Eq. (B7) (dotted lines) for high-yield conditions (lines with circles) and Z conditions. The magnetic pressure exceeds the radiation ablation pressure until about 6 ns prior to stagnation.

evant to a high-yield facility (60-MA peak load current, 250-eV peak radiation temperature). The temperature history uses the shape in Figure 5, which is representative of simulations before <75 ns (Chrien *et al.*, 1999) and measurements after 75 ns (Porter, 1997). We use the calculated wall albedo history as a function of time (see Fig. 6) to calculate the wall loss fraction $(1 - \alpha)$ as a function of time [Eqs. (B7) and (B8)]. The magnetic pressure is calculated from a measurement of load current (Stygar *et al.*, 1997). Figure 15 plots the ratio of magnetic to radiation ablation pressure (P_m/P_a) for both Z and high-yield conditions. The magnetic pressure exceeds the radiation ablation pressure of the Au wall by a factor of 2

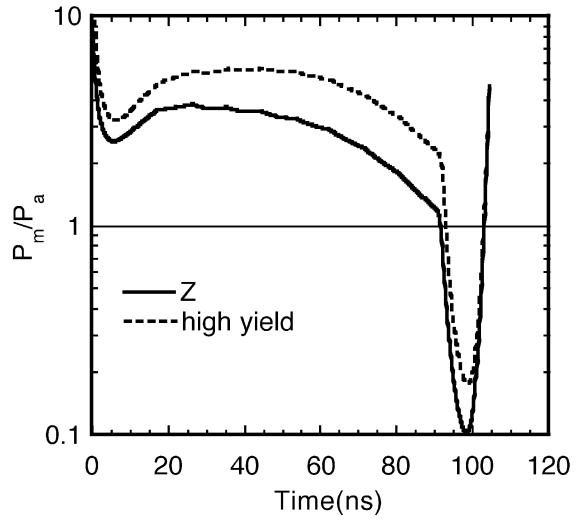

Fig. 15. Ratio of magnetic pressure to radiation ablation pressure for Z (solid line) and high yield conditions (dotted line).

to 4 during the first 90 ns of the implosion. This may explain why these small gaps are able to deliver current during the 100-ns pinch implosion time, even as the transmission line surfaces are bathed in radiation at more than 30 eV. The radiation pressure exceeds magnetic about 6.7 ns before the pinch stagnation for the Z parameters and 5.4 ns before for the high-yield parameters. P_m/P_a is increased during the pinch run-in phase, and the peak magnetic pressure is a larger fraction of the peak radiation pressure for the high yield case, in agreement with the scaling in Eq. (B10).

The temperature increases from 70 eV to 140 eV (for Z) in 7 ns following the time that the ablation pressure exceeds the magnetic pressure. Assume that the Au wall will freely expand across the magnetic field at the following rate during this period:

$$U_f \approx C_s = 3T_{\mathrm{heV}}^{0.8}\,\rho_{\mathrm{g/cm^3}}^{-0.07}\ \mathrm{cm}/\mu\mathrm{s}, \tag{B11}$$

using a result for C_s from Lindl (1995), where ρ is the Au mass density in grams per centimeter cubed. We estimate the range of Au mass density that will short the gap electrically (2.4×10^{-6} to 8.5×10^{-4} g/cm^3), or will close the gap to radiation leakage (3.1×10^{-3} to 4.8×10^{-3} g/cm^3) and thereby obtain a range of wall closure velocities which give estimates of AK gap closure times. An ion density of 2×10^{17} to 5×10^{19} cm^{-3} is sufficient to conduct 1–10 MA for 10 ns over the AK feed area and short the AK gap electrically. This occurs at an Au atom density of 7×10^{15} cm^{-3} to 3×10^{18} cm^{-3} [$\bar{Z} = 20$ to 27 at 70 eV to 140 eV from Eq. (B5) (Lindl, 1995)], which is an Au mass density of 2.4×10^{-6} to 8.5×10^{-4} g/cm^3. Equation (B11) then implies an effective Au flow velocity of 5 cm/μs to 13 cm/μs from both anode and cathode sides of the AK gap. A 2-mm gap thus shorts electrically in 9 ns to 20 ns at these velocities, within 2 ns to 13 ns after peak temperature. Assuming a length of the feed region of 0.1 to 0.5 cm, a Au mass density of $\rho = 3.1 \times 10^{-3}$ to 4.8×10^{-3} g/cm^3 is sufficient to provide an optical depth of 1 for outgoing hohlraum radiation (at 70 to 140 eV; see Eq. (A7), Lindl, 1995). The velocity of this surface is about 4 cm/μs to 8 cm/μs, blocking radiation flowing out of the 2-mm gap within about 12 ns to 23 ns, within 6 ns to 16 ns after peak temperature. Approximately 1.1 ± 0.6 mm of the 2-mm gap would fill with wall material at this range of velocities (8 cm/μs to 26 cm/μs two-sided closure) by peak temperature for Z conditions. Figure 14 shows that the magnetic pressure exceeds the ablation pressure for a somewhat longer period at high-yield conditions (1.3 ns). However, the velocity of the Au will be 60% faster at the higher temperatures. Equations (B11), (A7), and (8) show that the gap closure time scales as $d/(2C_s) \propto d/I^{0.38}$. Although 60% larger AK gaps (3–4 mm) may be required for high-yield conditions, this model indicates rapid closure of the Au wall limits radiation loss.

This simple scaling gives increased confidence in our ability to scale this system to levels relevant for high yield. More theoretical and experimental work must be done to characterize the behavior of this gap. Additional physics that may play a role are electron-driven expansion of material from the wall, cross-field motion of charged particles by kinetic effects, the balance of plasma erosion by current flow and resupply from wall ablation, cross-field motion of plasma by other instabilities, and $\mathbf{J} \times \mathbf{B}$ acceleration in the axial direction (self-clearing) of plasma material out of the gap.

https://doi.org/10.1017/S0263034601193055 Published online by Cambridge University Press